Self Energy effect in frequency dependent Vertex flow equation

D. Vilardi, C. Taranto, and W. Metzner
Max Planck Institute for Solid State Research, Stuttgart
(Dated: July 12, 2017)

blablabl ...

PACS numbers:

I. INTRODUCTION

- Much of the weak coupling momentum structure of the vertex (for the fermionic Hubbard model) is know by means of fRG,its frequency structure has been investigated much less.

- In recent years several results have been obtained for the single impurity Anderson model vertex, both on its own and as essential ingredient for diagrammatic extensions of DMFT. Citare: Rohringer, Kinza, Hafermann, Karrasch, Wentzell (and references therein) for the SIAM. Extensions of DMFT: DGA, DF, DMF2RG, Trilex, Quadrilex.

- A systematic study keeping into account the full frequency dependence and a physically motivated approximation for the momentum dependence, and including fluctuations in all channels is still lacking.

- Our results show the feasibility, and, in some respects, the necessity of a complete treatment of the frequency dependence of the vertex, whose impact is particularly large in methods that aim at strong coupling.

- We will confirm some results already foreseen by 11, who has shown a "forward scattering instability" already with a simpler frequency parametrization.

- With the study of the frequency dependence of the vertex we understand the appearance of a *scattering instability.*

- The d-wave superconductivity is reduced.

- The frequency dependent vertex allows to compute a frequency dependent self energy, often neglected in static fRG.

- We will show that the self-energy feedback in the flow equations is essential to guarantee the consistency between vertex and propagators in the flow equations.

- even a Fermi-liquid self-energy can qualitatively change the physical results.

II. FORMALISM

A. Model

The Hubbard model[1] describes spin-$\frac{1}{2}$ fermions with a density-density interaction:

$$\mathcal{H} = \sum_{i,j,\sigma} t_{ij} c^\dagger_{i,\sigma} c_{j,\sigma} + U \sum_i n_{i,\uparrow} n_{i,\downarrow} \tag{1}$$

where $c^\dagger_{i,\sigma}$ and $c_{i,\sigma}$ are, respectively, creation and annihilation operators for fermions with spin $\sigma =\uparrow,\downarrow$. We consider the two-dimensional case with square lattice and repulsive interaction $U > 0$ at finite temperature T and in the SU(2) spin-symmetric phase. The hopping amplitude is restricted to $t_{ij} = t$ for nearest neighbors, $t_{ij} = t'$ for next-to-nearest neighbors. We take $t \equiv 1$ as energy unit.

B. Flow equations

In the following paragraph we will give some details about the functional renormalization group[2,3], and we will clarify some notation issue about the vertex.

Generally speaking, the fRG allows to use the renormalization group idea in the functional integral formalism.

This is done by endowing the action with an additional dependence on a scale-parameter Λ:[2,3]

$$\mathcal{S}^\Lambda[\overline{\psi},\psi] = -(\overline{\psi}, {G_0^\Lambda}^{-1}\psi) + \mathcal{S}_{\rm int}, \tag{2}$$

where $\mathcal{S}_{\rm int}$ is the interaction part, and $(\overline{\psi},\psi)$ summarizes the summation over all the quantum numbers of the fermionic fields $\overline{\psi}$ and ψ. The scale dependence, acquired through the non-interacting propagator G_0^Λ, generates flow equations[4] (with known initial conditions) for functional integrals, like the effective action, the effective interaction, or the generating functional for the connected Green's function. The final result is recovered for some final Λ-value so that: $G_0^{\Lambda_{\rm f}} = G_0$, and the original action is restored.

We will apply this approach to the effective action, whose expansions into the fields generates the one-particle irreducible (1PI) functions. By expanding the functional flow equation, one obtains a hierarchy of flow

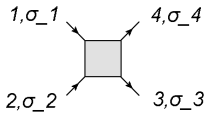

Figure 1: Notation of the two-particle vertex. **placeholder**

equations for the 1PI functions, involving vertices of arbitrarily high orders. We will restrict ourselves to the two-particle level truncation by retaining only the two lowest nonvanishing orders in the expansion, i.e., we consider the flow of the self-energy Σ^Λ and of the two-particle 1PI vertex V^Λ, neglecting the effects of higher order vertices. This truncation restricts the applicability of the approach to the weak-to-moderate coupling regime[5]. It can be furhter shown that, at the two-particle level trunctaion, the fRG sums up efficiently, although approximately, the so-called parquet-diagrams[6–8].

Due to translational invariance, we use the energy and momentum conservation to fix one of the arguments of the self-energy and of the vertex. Due to SU(2) symmetry, the self-energy is diagonal in spin-space:

$$\Sigma^\Lambda_{\sigma\sigma'}(k) = \Sigma(k)\delta_{\sigma,\sigma'}, \tag{3}$$

where $k = (\nu, \mathbf{k})$, ν is a fermionic Matsubara frequency and $\mathbf{k}$ a momentum in the first Brillouin zone.

For the notation of the two-particle vertex function $V_{\sigma_1\sigma_2\sigma_3\sigma_4}(k_1, k_2, k_3)$ we refer to Fig. 1, where $k_i = (\nu_i, \mathbf{k_i})$. The momentum $k_4 = k_1 + k_2 - k_3$ is fixed by conservation.Furthermore SU(2)-symmetry guarantees that the vertex does not vanish only for six spin combinations: $V^\Lambda_{\uparrow\uparrow\uparrow\uparrow} = V^\Lambda_{\downarrow\downarrow\downarrow\downarrow}$, $V^\Lambda_{\uparrow\downarrow\uparrow\downarrow} = V^\Lambda_{\downarrow\uparrow\downarrow\uparrow}$, and $V^\Lambda_{\uparrow\downarrow\downarrow\uparrow} = V^\Lambda_{\downarrow\uparrow\uparrow\downarrow}$. Finally, due to SU(2) symmetry and crossing relation one has:[9]

$$\begin{aligned} V^\Lambda_{\uparrow\uparrow\uparrow\uparrow}(k_1,k_2,k_3) &= V^\Lambda_{\uparrow\downarrow\uparrow\downarrow}(k_1,k_2,k_3) \\ &- V^\Lambda_{\uparrow\downarrow\uparrow\downarrow}(k_1,k_2,k_1+k_2-k_3), \quad (4)\\ V^\Lambda_{\uparrow\downarrow\downarrow\uparrow}(k_1,k_2,k_3) &= -V^\Lambda_{\uparrow\downarrow\uparrow\downarrow}(k_1,k_2,k_1+k_2-k_3). \quad (5)\end{aligned}$$

This allows us to consider only one function of three arguments for the vertex: $V^\Lambda(k_1,k_2,k_3) \equiv V^\Lambda_{\uparrow\downarrow\uparrow\downarrow}(k_1,k_2,k_3)$, all the others spin components being obtained by Eqns. (4-5).

With these considerations the flow equation for the self energy[2] reads:

$$\frac{d}{d\Lambda}\Sigma^\Lambda(k) = -\int_p S^\Lambda(p)\left[2V^\Lambda(k,p,p) - V^\Lambda(k,p,k)\right], \tag{6}$$

with $p = (\omega, \mathbf{p})$ and $k = (\nu, \mathbf{k})$. We use the notation $\int_p = T\sum_\omega \int_{\mathbf{p}}$, $\int_{\mathbf{q}} = \int \frac{d\mathbf{q}}{4\pi^2}$ being the normalized integral over the first Brillouin zone.

$$S^\Lambda = \left.\frac{dG^\Lambda}{d\Lambda}\right|_{\Sigma=\text{const}} \tag{7}$$

is the single-scale propagator and $G^{\Lambda^{-1}} = \left[(G^\Lambda_0)^{-1} - \Sigma^\Lambda\right]$ is the full propagator.

The vertex flow equation[2,10] can be written as:

$$\frac{d}{d\Lambda}V^\Lambda(k_1,k_2,k_3) = \mathcal{T}^\Lambda_{\text{pp}}(k_1,k_2,k_3) + \mathcal{T}^\Lambda_{\text{ph}}(k_1,k_2,k_3) + \mathcal{T}^\Lambda_{\text{phc}}(k_1,k_2,k_3), \tag{8}$$

where:[21]

$$\begin{aligned}\mathcal{T}^\Lambda_{\text{pp}}(k_1,k_2,k_3) &= -\frac{1}{2}\int_p \mathcal{P}^\Lambda(p,k_1+k_2-p)\Big\{V^\Lambda(k_1,k_2,k_1+k_2-p)V^\Lambda(k_1+k_2-p,p,k_3) \quad (9)\\ &\quad + V^\Lambda(k_1,k_2,p)V^\Lambda(p,k_1+k_2-p,k_3)\Big\};\\ \mathcal{T}^\Lambda_{\text{ph}}(k_1,k_2,k_3) &= -\int_p \mathcal{P}^\Lambda(p,k_3-k_1+p)\Big\{2V^\Lambda(k_1,k_3-k_1+p,k_3)V^\Lambda(p,k_2,k_3-k_1+p) \quad (10)\\ &\quad - V^\Lambda(k_1,k_3-k_1+p,p)V^\Lambda(p,k_2,k_3-k_1+p) - V^\Lambda(k_1,k_3-k_1+p,k_3)V^\Lambda(k_2,p,k_3-k_1+p)\Big\};\\ \mathcal{T}^\Lambda_{\text{phc}}(k_1,k_2,k_3) &= \int_p \mathcal{P}^\Lambda(p,k_2-k_3+p)V^\Lambda(k_1,k_2-k_3+p,p)V^\Lambda(p,k_2,k_3). \quad (11)\end{aligned}$$

Here we have defined the quantity:

$$\mathcal{P}^\Lambda(p,Q+p) = G^\Lambda(p)S^\Lambda(Q+p) + G^\Lambda(p+Q)S^\Lambda(p), \tag{12}$$

which is the scale-derivative, at fixed self energy, of a Green's function bubble with frequency and momentum transfer Q.

III. VERTEX APPROXIMATION

In order to deal with the frequency and momentum dependence of the vertex, we start by decomposing it as follows:

$$V^{\Lambda}(k_1,k_2,k_3) = U - \phi_{\rm p}^{\Lambda}(k_1+k_2;k_1,k_3) + \phi_{\rm m}^{\Lambda}(k_3-k_1;k_1,k_2) + \frac{1}{2}\phi_{\rm m}^{\Lambda}(k_2-k_3;k_1,k_2) - \frac{1}{2}\phi_{\rm c}^{\Lambda}(k_2-k_3;k_1,k_2), \quad (13)$$

Substituting Eq. (13) in Eq. (8) we obtain:

$$-\dot{\phi}_{\rm p}^{\Lambda}(k_1+k_2;k_1,k_3) + \dot{\phi}_{\rm m}^{\Lambda}(k_3-k_1;k_1,k_2) + \frac{1}{2}\dot{\phi}_{\rm m}^{\Lambda}(k_2-k_3;k_1,k_2) - \frac{1}{2}\dot{\phi}_{\rm c}^{\Lambda}(k_2-k_3;k_1,k_2) = \mathcal{T}_{\rm pp}^{\Lambda}(k_1,k_2,k_3) + \mathcal{T}_{\rm ph}^{\Lambda}(k_1,k_2,k_3) + \mathcal{T}_{\rm phc}^{\Lambda}(k_1,k_2,k_3). \quad (14)$$

We associate the momentum transfer argument of $\mathcal{P}^{\Lambda}$ in Eqns. (9-11) to the momentum transfer argument of the $\phi_{\rm x}$ on the right hand side of Eq. 13. This way, it is easy to attribute $\mathcal{T}_{\rm pp}^{\Lambda}$ to the flow equation of the only function in Eq. (14) that depends explicitly on k_1+k_2: $-\dot{\phi}_{\rm p}^{\Lambda} = \mathcal{T}_{\rm pp}^{\Lambda}$. The same is true for the particle hole crossed channel: $\mathcal{T}_{\rm phc}^{\Lambda} = \dot{\phi}_{\rm m}^{\Lambda}$. We associate to the particle-hole diagram the third and fourth term on the left hand side of Eq. (14): $\mathcal{T}_{\rm ph}^{\Lambda}(k_1,k_2,k_3) = \frac{1}{2}\dot{\phi}_{\rm m}^{\Lambda}(k_2-k_3;k_1,k_2) - \frac{1}{2}\dot{\phi}_{\rm c}^{\Lambda}(k_2-k_3;k_1,k_2)$. Hence the flow equations for ϕ then read:

$$\dot{\phi}_{\rm p}^{\Lambda}(Q;k_1,k_3) = -\mathcal{T}_{\rm pp}^{\Lambda}(k_1,Q-k_1,k_3), \quad (15)$$

$$\dot{\phi}_{\rm c}^{\Lambda}(Q;k_1,k_2) = -2\mathcal{T}_{\rm ph}^{\Lambda}(k_1,k_2,Q+k_1) + \mathcal{T}_{\rm phc}^{\Lambda}(k_1,k_2,Q+k_1), \quad (16)$$

$$\dot{\phi}_{\rm m}^{\Lambda}(Q;k_1,k_2) = \mathcal{T}_{\rm phc}^{\Lambda}(k_1,k_2,Q+k_1), \quad (17)$$

where $Q=(\Omega,\mathbf{Q})$ is a frequency and momentum transfer.

Following Refs. 10,11, we address first the momentum dependence. To this end, we introduce a decomposition of the unity by means of a set of orthonormal form factors for the two fermionic momenta $\{f_l(\mathbf{k})\}$ obeying the completeness relation:

$$\int_{\mathbf{k}} f_l(\mathbf{k}) f_m(\mathbf{k}) = \delta_{l,m}. \quad (18)$$

The procedure outlined here is described in detail, e.g., in Ref. 12.

We can then project each channel on a subset of form factors, whose choice is physically motivated[10]. Let us stress that the if one could keep all the form factors the expansion would be exact.

For the pairing channel we keep only $f_s(\mathbf{k}) = 1$ and $f_d(\mathbf{k}) = \cos k_x - \cos k_y$:

$$\phi_{\rm p}^{\Lambda}(Q;k_1,k_3) = \mathcal{S}_{\mathbf{Q}}^{\Omega;\nu_1,\nu_3} + f_d\left(\frac{\mathbf{Q}}{2}-\mathbf{k}_1\right) f_d\left(\frac{\mathbf{Q}}{2}-\mathbf{k}_3\right) \mathcal{D}_{\mathbf{Q}}^{\Omega;\nu_1,\nu_3}. \quad (19)$$

The divergence in the channel $\mathcal{S}$ is associated to the emergence of s-wave superconductivity, while $\mathcal{D}$ to d-wave superconductivity.[2,3]

For the charge and magnetic channels we restrict ourselves to $f_s(\mathbf{k}) = 1$ only:

$$\phi_{\rm c}^{\Lambda}(Q;k_1,k_2) = \mathcal{C}_{\mathbf{Q}}^{\Omega;\nu_1,\nu_2}, \quad (20)$$

$$\phi_{\rm m}^{\Lambda}(Q;k_1,k_2) = \mathcal{M}_{\mathbf{Q}}^{\Omega;\nu_1,\nu_2}, \quad (21)$$

corresponding to instabilities in the charge and magnetic channels, respectively (for notation simplicity we omit the Λ-dependencies of the channel functions $\mathcal{S}$, $\mathcal{D}$, $\mathcal{C}$ and $\mathcal{M}$).

Let us stress that for each channel in Eq. (13) we have defined *its own* frequency notation, consisting of one transfer frequency in the specific channel and two remaining independent fermionic frequencies. At finite temperature these frequency transfer is a bosonic Matsubara frequency.

The choice of the mixed notation is the most natural[13] since the transferred momentum and frequency play a special role in the diagrammatics. Indeed, it is the only dependence generated in second order perturbation theory and the main dependence in finite order perturbation theory. This notation is also convenient to express the Bethe-Salpeter equations[9], which are deeply related to parquet-approximations and fRG.

Although one expects a leading dependence in the bosonic frequency, in particular in the weak coupling regime, we will see that in some cases the dependence on fermionic frequencies can become strong and not negligible.

In Refs. 10, with a simplified frequency dependence, the channel functions above are interpreted as bosonic exchange propagators. Such an interpretation is missing with full frequency-dependence.

The flow equations for the channels $\mathcal{S}$, $\mathcal{D}$, $\mathcal{C}$ and $\mathcal{M}$ can be derived from the projection onto form factors of

Eq. (9)-(11):

$$\dot{\mathcal{S}}_{\mathbf{Q}}^{\Omega;\nu_1,\nu_3} = -\int_{\mathbf{k}_1,\mathbf{k}_3} \mathcal{T}_{\rm pp}(k_1, Q-k_1, k_3); \quad (22)$$

$$\dot{\mathcal{D}}_{\mathbf{Q}}^{\Omega;\nu_1,\nu_3} = -\int_{\mathbf{k}_1,\mathbf{k}_3} f_d\left(\frac{\mathbf{Q}}{2}-\mathbf{k}_1\right) f_d\left(\frac{\mathbf{Q}}{2}-\mathbf{k}_3\right) \mathcal{T}_{\rm pp}(k_1, Q-k_1, k_3); \quad (23)$$

$$\dot{\mathcal{C}}_{\mathbf{Q}}^{\Omega;\nu_1,\nu_2} = \int_{\mathbf{k}_1,\mathbf{k}_2} \mathcal{T}_{\rm phc}(k_1, k_2, Q+k_1) - 2\mathcal{T}_{\rm ph}(k_1, k_2, k_2-Q); \quad (24)$$

$$\dot{\mathcal{M}}_{\mathbf{Q}}^{\Omega;\nu_1,\nu_2} = \int_{\mathbf{k}_1,\mathbf{k}_2} \mathcal{T}_{\rm phc}(k_1, k_2, Q+k_1). \quad (25)$$

The final equations are then obtained by substituting the decomposition (13) into the equations above, and using trigonometric equalities. As an example we report here the equation for the magnetic channel, while the expression for the other channels are reported in the Appendix:

$$\dot{\mathcal{M}}_{\mathbf{Q}}^{\Omega;\nu_1,\nu_2} = \sum_{\nu} L_{\rm m\,\mathbf{Q}}^{\Omega;\nu_1,\nu} P_{\mathbf{Q}}^{\Omega,\nu} L_{\rm m\,\mathbf{Q}}^{\Omega;\nu,\nu_2-\Omega}, \quad (26)$$

with:

$$P_{\mathbf{Q}}^{\Omega;\omega} = \int_{\mathbf{p}} G^{\Lambda}_{\mathbf{p},\omega} S^{\Lambda}_{\mathbf{Q}+\mathbf{p},\Omega+\omega} + G^{\Lambda}_{\mathbf{Q}+\mathbf{p},\Omega+\omega} S^{\Lambda}_{\mathbf{p},\omega}, \quad (27)$$

and:

$$\begin{aligned} L_{\rm m\,\mathbf{Q}}^{\Omega;\nu_1,\nu_2} &= U + \mathcal{M}_{\mathbf{Q}}^{\Omega;\nu_1,\nu_2} \\ &+ \int_{\mathbf{p}} \Big\{ -\mathcal{S}_{\mathbf{p}}^{\nu_1+\nu_2;\nu_1,\nu_1+\Omega} \\ &-\tfrac{1}{2}\ \mathcal{D}_{\mathbf{p}}^{\nu_1+\nu_2;\nu_1,\nu_1+\Omega}[\cos(Q_x)+\cos(Q_y)] \\ &+\tfrac{1}{2}\ \left[\mathcal{M}_{\mathbf{p}}^{\nu_2-\nu_1-\Omega;\nu_1,\nu_2} - \mathcal{C}_{\mathbf{p}}^{\nu_2-\nu_1-\Omega,\nu_1,\nu_2}\right]\Big\} \end{aligned} \quad (28)$$

Let us notice that after the momentum integrals in P and L are performed, the right hand side can be expressed as a matrix-matrix multiplication in frequency space, where Ω and $\mathbf{Q}$ appear as parameters.

After this decomposition, the evaluation of vertex-flow equation, depending on six arguments, is reduced to the flow of the four functions $\mathcal{S}$, $\mathcal{D}$, $\mathcal{C}$, $\mathcal{M}$ each of them depending on three frequencies and one momentum only. In order to compute these equations numerically we needed to discretize the momentum dependence on patches covering the Brillouin zone and to truncate the frequency dependence to some maximal frequency value. More details about this are given in the Appendix.

Let us stress that, while the form-factor projection procedure is well defined in momentum space, a similar approximation for the frequency, i.e., reducing the vertex frequency dependence to a frequency transfer only[11,14,15], is more problematic. Indeed this projection in frequency space requires that the two remaining frequencies are chosen arbitrarily. This choice affects quantitatively and qualitatively the results, for reasons that are clear looking at the frequency structure of the vertex, discussed below.

A. Cutoff scheme

To use the flow equations defined above we need to specify the Λ-dependence of the non interacting propagator G_0^{Λ}, often referred to as *cutoff scheme*, in connection to the scale-separation of the renormalization group. In the rest of the paper we have used two different cutoffs.

For most our calculations we have used the *Interaction cutoff*, introduced in Ref. 16:

$$G_0^{\Lambda}(k) = \Lambda G_0(k) = \frac{\Lambda}{i\nu - \mu - \varepsilon_{\mathbf{k}}}, \quad (29)$$

Where the scale-parameter Λ flows from 0 to 1, and with $\varepsilon_{\mathbf{k}} = -2t[\cos(k_x)+\cos(k_y)] - 4t'\cos(k_x)\cos(k_y)$. μ is the chemical potential needed to fix the occupation at the desired value n. ν is a fermionic Matsubara-frequency: $\nu = \frac{\pi}{\beta}(2m+1)$, $m \in \mathbb{Z}$. $\beta = 1/T$ is the inverse temperature. Correspondingly the interacting Green's function reads:

$$G^{\Lambda}(k) = \frac{\Lambda}{i\nu - \varepsilon_{\mathbf{k}} - \mu - \Lambda\Sigma^{\Lambda}(k)} \quad (30)$$

We have introduced a Λ-dependent chemical potential to maintain the occupation fixed during the flow. The chemical potential becomes a functional of the flowing self-energy, $\mu = \mu[\Sigma^{\Lambda}]$, whose value is found by solving the equation:

$$n = n^{\Lambda}(\mu) \equiv \int_k \frac{e^{i\nu 0^+}}{i\nu - \varepsilon_{\mathbf{k}} - \mu - \Lambda\Sigma^{\Lambda}(k)}. \quad (31)$$

for μ.

The main advantage of the interaction cutoff is that the Λ-dependent action can be interpreted[16] as the physical action of the system with rescaled interaction $\tilde{U}^{\Lambda} = \Lambda^2 U$.

Since T acts as an infrared cutoff, for our purposes we do not need to worry about the fact that this cutoff is not scale-selective, and hence does not regularize possible divergences in the bubbles. Furthermore it has been shown in Ref. 17 that, in the context of the single-impurity Anderson model, the vertex-structures do not depend qualitatively on the cutoff-choice, and the specific effect of the interaction-cutoff on the vertex frequency structure has been studied in detail.

As a benchmark for the robustness of our results on the cutoff-choice, we have used a soft version of the*frequency selective cutoff* defined[18] by:

$$G_0^{\Lambda}(k) = \frac{1}{i\,\mathrm{sign}\sqrt{\nu^2+\Lambda^2} - \mu - \varepsilon_{\mathbf{k}}}, \quad (32)$$

with $\Lambda_0 = \infty$ and $\Lambda_{\rm f} = 0$. Also in this case we have performed our calculations at fixed occupation.

For both our cutoff choices at the beginning of the flow one has $G_0^{\Lambda_0} = 0$, corresponding to a initial conditions for the self-energy and the vertex defined by, $\Sigma^{\Lambda_0} = 0$ and $V^{\Lambda_0} = U$.

IV. RESULTS

A. Frequency dependence of Vertex

In the next section, we present our result obtained by full frequency dependent fRG. All the results are presented in units of $t = 1$. **should we write this? repetita iuvat?**

Numerical implementation We have implemented numerically the flow equations reported in the appendix.

Due to the different nature of the momentum arguments of self-energy and vertex we have defined two different patching of the irreducible Brillouin zone. Similarly to what is done in Ref. 10, the vertex patching describes more accurately the corners around $(0, 0)$ and (π, π), where the instability vectors are expected for our system.

The situation is completely different for the self-energy, for which the most relevant physics happens in the vicinity of the Fermi surface. Therefore we concentrate the patches along the Fermi surface and in its immediate vicinity (see Fig. 9 and Fig. 10), with some further care close to the "antinodal" points near $(\pi, 0)$, relevant for antiferromagnetism.

In the calculations presented in the following we have used 29 patches for the vertex and 44 for the self-energy.

For the practical implementation of the frequency dependence we found convenient to rewrite $\mathcal{S}$, $\mathcal{D}$, $\mathcal{C}$ and $\mathcal{M}$ as function of three bosonic frequencies. For each frequency argument we restricted ourselves to at least 40 positive and 40 negative Matsubara frequencies. We stress that the number of Matsubara frequencies that can be taken into account in the calculation sets the lowest reachable temperature.

B. Instabilities analysis

By means of fRG one can perform an instability analysis of the system: for some value of the cutoff Λ one of the channels shows a divergence. The cutoff scale Λ_c for which this happens is called *critical scale*, and from the diverging channel one can evince the leading instability of the system. In Fig. 2 we show the critical scale $1 - \Lambda_c$ as a function of the doping $x = 1 - n$ with and without self-energy feedback, for $T = 0.08t$, $t' = -0.32t$ and $U = 4t$. We show our result as function of $1 - \Lambda$, which vanishes at the end of the flow. For the physical interpretation, we can refer, instead, to the rescaled interaction[16] $\tilde{U}^\Lambda$ as discussed in Sec.**??**.

The critical value has been defined as the scale for which the value of the larger channels exceeds $200t$. We have checked that for these stopping values the flow of the largest channel begins to increase stronger than exponentially. These results are also consistent with an instability analysis based on the susceptibilities.

A divergence in the vertex signals a symmetry breaking at finite temperature. This is a consequence of the truncation scheme, that does not respect the Mermin-Wagner theorem[19]. The presence of a finite critical scale in the pure fermionic fRG signals the appearance of strong bosonic fluctuations that cannot be treated within the approximation-scheme we are using.[5] Even though the flow cannot be continued beyond the critical scale, from the analysis of vertex and self-energy we can identify the more relevant interactions of the system.

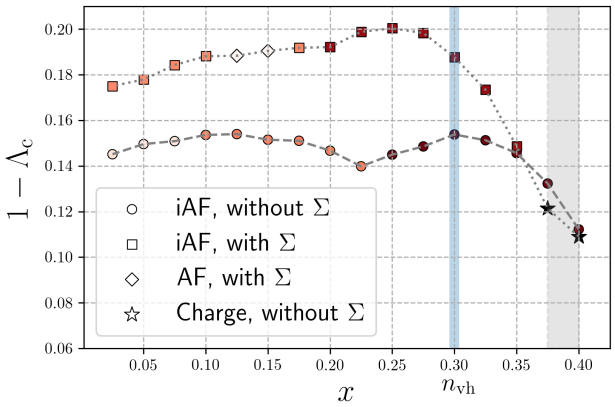

Figure 2: Critical scale $1 - \Lambda_c$ as a function of the doping $x = 1 - n$, for $T = 0.08t$, $t' = -0.32t$ and $U = 4t$. Square symbols and circles refer to incommensurate antiferromagnetism (iAF), respectively without and with self-energy feedback. The black stars refer to a divergence in the charge channel (forward scattering in Ref. 11). The color of squares and circles encodes the distance of the incommensurability vector from (π, π): darker color corresponds to higher incommensurability. The vertical light blue line marks the van Hove filling.

For the parameter sets shown in Fig. 2 and without self-energy feedback (square and star symbols), there are two possible instabilities. For doping smaller than 0.35 the leading fluctations of the system are either commensurate or incommensurate antiferromagnetic. The incommensurability δ is defined through $\mathbf{Q} = (\pi, \pi - \delta)$, where the magnetic channel $\mathcal{M}^\Lambda$ has its maximum for momentum $\mathbf{Q}$. The value of δ is encoded in the color of the symbols, where darker colors corresponds to larger δ, reaching the value of $\delta = 1.13$ for doping x between 0.25 and 0.35. The region of commensurate antiferromagnetism for $0.125 \leq x \leq 0.150$ has to be attributed to the presence of a large plateu around (π, π) in the bare bubble. Correspondingly the magnetic susceptibility is enhanced in all the region around (π, π), and the commensurate peak coexists with incommensurate ones of similar magnitude.

The most striking feature is the presence of a divergence in the charge channel $\mathcal{C}^\Lambda$ for larger values of doping, marked in Fig. 2 by black stars. This feature was already observed by Husemmann *et al.* in Ref. 10, where it was named "forward scattering instability". Unlike the magnetic channel, the charge channel $\mathcal{C}^\Lambda$ diverges for

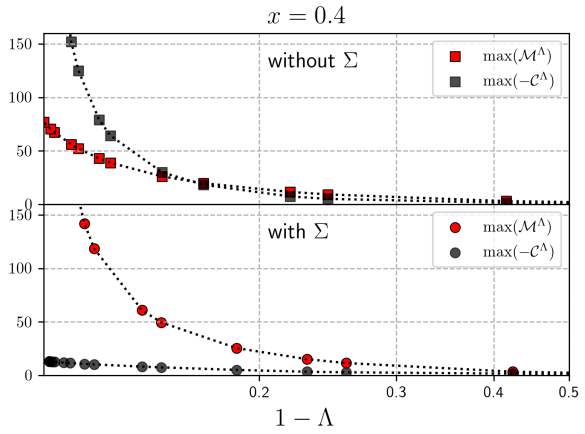

Figure 3: Flow of the maximal value of the charge ($\mathcal{C}$) and magnetic ($\mathcal{M}$) channels as functions of Λ, for $x = 0.4$, $t' = -0.32$, $U = 4t$ and $T = 0.08t$. Top: without self-energy feedback; bottom: with self-energy feedback.

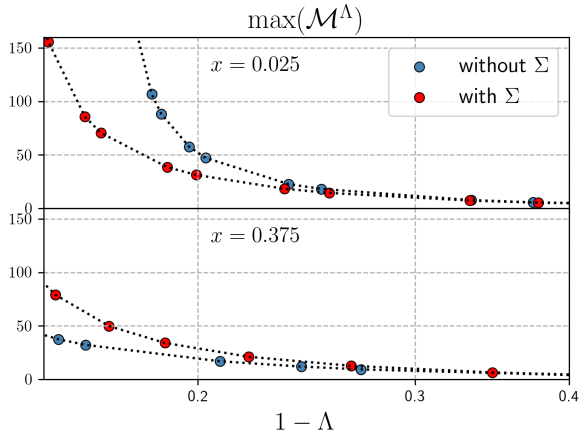

Figure 4: Flow of the maximal value of the magnetic ($\mathcal{M}$) channel as functions of Λ, for $x = 0.025$ (top) and $x = 0.375$ (bottom). The other parameters are $t' = -0.32$, $U = 4t$ and $T = 0.08t$. Red symbols: with self-energy feedback; blue symbols: without self-energy feedback.

a finite frequency transfer $\Omega = 2\pi/\beta$, which makes the interpretation of the divergence in terms of a physical instability not obvious. The frequency structure of the divergent charge channel $\mathcal{C}^\Lambda$ and its origin, will be discussed further in paragraph **??**.

Including the self-energy feedback results in three effects, as can be seen from the circular symbols in Fig. 2 . First, the self-energy feedback decreases $1 - \Lambda_c$. Second, the incommensurability vector is also affected, the region of commensurate antiferromagnetism disappears, and one can observe a more regular trend of increasing δ as the doping is increased. Third, the divergence in the charge channel is completely suppressed, and the leading instability in the doping region $0.375 \leq x \leq 0.4$ remains of the incommensurate antiferromagnetic type. This can

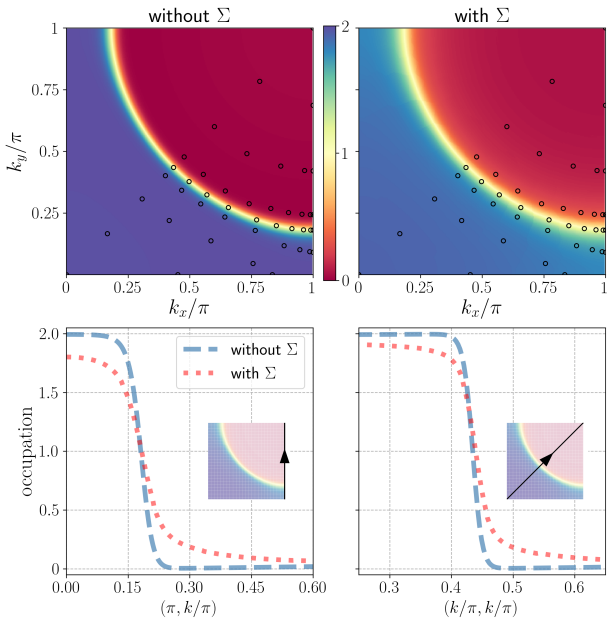

Figure 5: **placeholder**

be also be seen from Fig. 3, where we compare the flow of the maximum (of the absolute value) of magnetic and charge channel with and without the self-energy feedback for doping $x = 0.4$. Without self-energy feedback, the charge channel rapidly starts to increase, taking large and negative values. Due to the charge channel feedback the magnetic channel is reduced. The effect of the self-energy to the charge channel is evident, as can be seen from the bottom inset: the charge channel does not diverge during the flow, and it is strongly damped. At the same time the magnetic channel is enhanced.

This is confirmed by Fig. 4, where we show the maximum of $\mathcal{M}$ with and without self-energy feedback for $x = 0.025$ (top inset) and $x = 0.375$ (bottom inset). One can see that the enhancement of $\mathcal{M}$ due to self-energy is specific of the large doping region, while, in the small doping region the self energy decreases $\mathcal{M}$. Hence the self-energy affects the magnetic channel either directly, reducing the particle-hole bubble (for small doping), or indirectly through the feedback of other channels, i.e., reducing the charge channel at large doping.

To understand better these effects we looked for possible changes in the Fermi surface structure, analyzing the momentum resolved occupation, computed as:

$$n(\mathbf{k}) = \frac{2}{\beta} \sum_\nu \frac{e^{i\nu 0^+}}{i\nu - \varepsilon_{\mathbf{k}} - \mu^\Lambda - \Lambda\Sigma^\Lambda(\mathbf{k}, i\nu)}, \tag{33}$$

where the factor 2 accounts for the spin degree of freedom. In Fig. 6 we show the non interacting (top left) and interacting (top right) occupation in the first quadrant of the Brillouin zone for doping $x = 0.025$. The former is

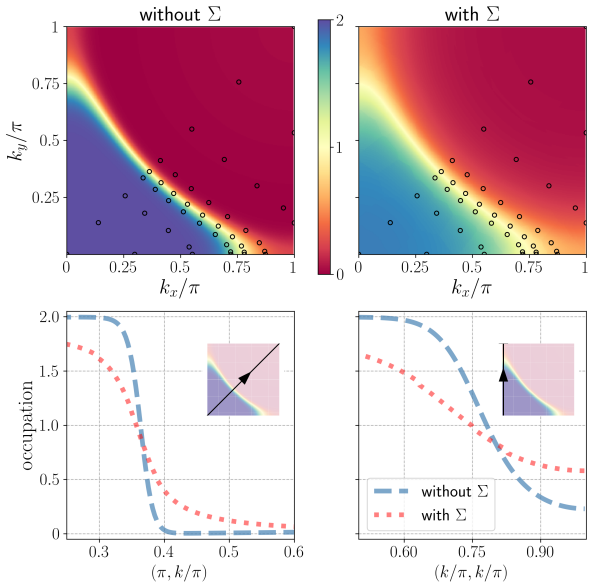

Figure 6: **placeholder** here we will write a lot of useful comments about the figure and I will add a lot of

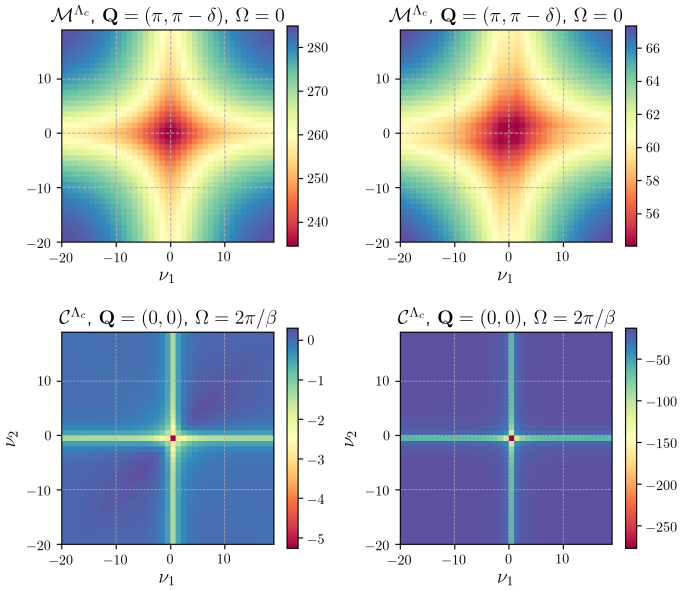

Figure 7: Frequency structure of the charge channel $\mathcal{C}^{\Lambda}_{\Omega,\mathbf{Q}}(\nu_1, \nu_2)$ (on the left) and of the magnetic channel $\mathcal{M}^{\Lambda}_{\Omega,\mathbf{Q}}(\nu_1, \nu_2)$ (on the right), for $x = 0.4$, $t' = -0.32$, $U = 4t$ and $T = 0.08t$ and without self-energy, corresponding to the rightmost point in Fig. 2. Both channels are plotted for the frequency and momentum transfer for which they have their maximum. Note that the frequency transfer for $\mathcal{C}^{\Lambda}_{\Omega,\mathbf{Q}}$ is the first bosonic Matsubara frquency $2\pi/\beta$. The value of δ is 1.13.

computed by setting $\Sigma^{\Lambda} = 0$ (and non interacting chemical potential) in Eq.(33), while the latter is computed at the critical scale Λ_c. The non interacting Fermi surface broadening is only due to finite temperature.

Comparing the two panels, one does not observe any relevant shift of the Fermi surface location, but the Fermi surface broadening is appreciably larger in the interacting case, due to self-energy. Similar considerations apply for doping $x = 0.4$, as one can see from Fig. 5, where the broadening is even more evident.

C. Vertex frequency dependence

We focus now on the frequency dependence of the channels. In particular we will look at the channels that show a divergence, i.e., the charge and the magnetic observed in Fig. 2, while we refer to the Appendix for the superconducting ones.

As mentioned in the previous section the divergence of the charge and magnetic channel are different. The charge channel diverges for a finite frequency transfer and only when we neglect the self-energy feedback. We will further argue here that the two divergences are also of physical different origin.

While the dependence on the transfer momentum and frequency $(\mathbf{Q}, \Omega)$ has already been studied, here we focus on the dependence on the fermionic frequencies ν_1 and ν_2. Therefore we present different color plots for fixed $(\mathbf{Q}, \Omega)$, showing the dependence on the fermionic frequencies.

In the top left panel of Fig. 7 we show the magnetic channel $\mathcal{M}^{\Lambda_c}_{\mathbf{Q}\Omega}(\nu_1, \nu_2)$ in the small doping region, where antiferromagnetism is leading. The case shown has been calculated with self-energy feedback, but we notice that the frequency structures we discuss do not depend strongly on the self-energy feedback. For clarity we restrict the plots to the first 20 positive and negative Matsubara frequencies, and we notice that larger frequencies can be deduced by the asymptotic.**??** It is easy to see that the fRG equations are equivalent to RPA when only one channel is taken into account. The magnetic channel calculated with RPA would depend only on the frequency and momentum transfer, that would result, for the plot shown, in a completely constant color. Hence any variation in the frequency structure has to be ascribed to the presence of the other channels in fRG. As already observed in the literature *who should we cite*, the channel competition suppresses the magnetic channel. This is clear in two ways:the largest value of $\mathcal{M}$ is decreased compared to RPA, and the frequency structure at the center is negative compared to the asymptotic value.

In the bottom left panel of Fig. 7 we show the charge channel $\mathcal{C}^{\Lambda_c}_{\mathbf{Q},\Omega}(\nu_1, \nu_2)$ for the same parameter set as before, but for finite frequency transfer $\Omega = 2\pi/\beta$, important for the forward scattering instability. The frequency

structure is completely different from the case described above. The channel assumes negative values, and the maximum is for frequencies $\nu_1 = \pi/\beta$ and $\nu_2 = -\pi/\beta$. This structure cannot be explained in terms of standard ladder diagrams, and might be also related to the behavior of the retarded interaction described by[?] .

In the two right panels of Fig. **??** we show the same quantities but for $x = 0.4$, without self-energy feedback, for which the charge channel has the largest absolute value. The frequency structure are similar to the one described above. However the maximum (in absolute value) observed in the charge channel is very localized, unlike for the magnetic channel in the iAF case.

Perpendicular ladder

- Introduce perpendicular ladder (PL) for charge.
- Colorplot of charge in PL.
- Discuss the role of the Bubble at $\boldsymbol{Q} = (0, 0)$ and plot it as a function of ν.

All these considerations suggest that the divergence of the charge channel is rather an artefact of fRG without self-energy, arising from a lack of consistence between the vertex and the Green's function in the flow equations. In the next section we further substanciate this conclusion, by explaining the mathematical origin of the feature. The self-energy has qualitative and quantitive effects on the flow equations: quantitively

D. Self energy analysis

- With self energy feedback, we didn't find any charge instability problem for any parameters range studied.
- Plot of the Fermi surface based patch scheme.
- Plot of $\Sigma(i\omega)$ at $\boldsymbol{k} = (\pi, 0)$, $\boldsymbol{k} = \boldsymbol{k}_{HS}$ and $\boldsymbol{k} = (\pi/2, \pi/2)$ in frequency space.
- Plot of $Z_{\boldsymbol{k}}$
- Plot of occupation with and without Σ

V. CONCLUSIONS

- order of the paragraph? shall we discuss first self energy or vertex?
- do we want to show more vertex structure in the appendix?

Acknowledgments

We thank for valuable discussions .... This research was supported by.

VI. APPENDICES

A. Flow equations

For practical reason, from now on, we omit the esplicit Λ dependencies. The flow equation for the $\mathcal{S}$ channel read:

$$\dot{\mathcal{S}}^{\Omega;\nu_1,\nu_3}_{\mathbf{Q}} = \frac{1}{2}\sum_{\nu} L_{\mathrm{s}}{}^{\Omega;\nu_1,\nu}_{\mathbf{Q}} P^{\Omega,\nu}_{\mathrm{s},\mathbf{Q}} L_{\mathrm{s}}{}^{\Omega;\nu,\Omega-\nu_3}_{\mathbf{Q}} + \frac{1}{2}\sum_{\nu} L_{\mathrm{s}}{}^{\Omega;\Omega-\nu_1,\nu}_{\mathbf{Q}} P^{\Omega,\nu}_{\mathrm{s},\mathbf{Q}} L_{\mathrm{s}}{}^{\Omega;\nu,\nu_3}_{\mathbf{Q}}, \tag{34}$$

with:

$$P^{\Omega;\omega}_{\mathbf{Q}} = \int_{\mathbf{p}} G_{\mathbf{p},\omega} S_{\mathbf{Q}-\mathbf{p},\Omega-\omega} + G_{\mathbf{Q}-\mathbf{p},\Omega-\omega} S_{\mathbf{p},\omega}, \tag{35}$$

and:

$$L_{\mathrm{s}}{}^{\Omega;\nu_1,\nu_3}_{\mathbf{Q}} = U - \mathcal{S}^{\Omega;\nu_1,\nu_3}_{\mathbf{Q}} + \int_{\mathbf{p}} \Big[\mathcal{M}^{\nu_3-\nu_1;\nu_1,\Omega-\nu_1}_{\mathbf{p}} + \frac{1}{2}\mathcal{M}^{\Omega-\nu_1-\nu_3;\nu_1,\Omega-\nu_1}_{\mathbf{p}} - \frac{1}{2}\mathcal{C}^{\Omega-\nu_1-\nu_3;\nu_1,\Omega-\nu_1}_{\mathbf{p}}\Big]. \tag{36}$$

The flow for the $\mathcal{D}$ channel read:

$$\dot{\mathcal{D}}^{\Omega;\nu_1,\nu_3}_{\mathbf{Q}} = \frac{1}{2}\sum_{\nu} L_{\mathrm{d}}{}^{\Omega;\nu_1,\nu}_{\mathbf{Q}} P^{\Omega,\nu}_{\mathrm{d},\mathbf{Q}} L_{\mathrm{d}}{}^{\Omega;\nu,\Omega-\nu_3}_{\mathbf{Q}} + \frac{1}{2}\sum_{\nu} L_{\mathrm{d}}{}^{\Omega;\Omega-\nu_1,\nu}_{\mathbf{Q}} P^{\Omega,\nu}_{\mathrm{d},\mathbf{Q}} L_{\mathrm{d}}{}^{\Omega;\nu,\nu_3}_{\mathbf{Q}}, \tag{37}$$

with:

$$P^{\Omega;\omega}_{\mathrm{d},\mathbf{Q}} = \int_{\mathbf{p}} f_{\mathrm{d}}\left(\frac{\mathbf{Q}}{2} - \mathbf{p}\right)^2 \left[G_{\mathbf{p},\omega} S_{\mathbf{Q}-\mathbf{p},\Omega-\omega} + G_{\mathbf{Q}-\mathbf{p},\Omega-\omega} S_{\mathbf{p},\omega}\right], \tag{38}$$

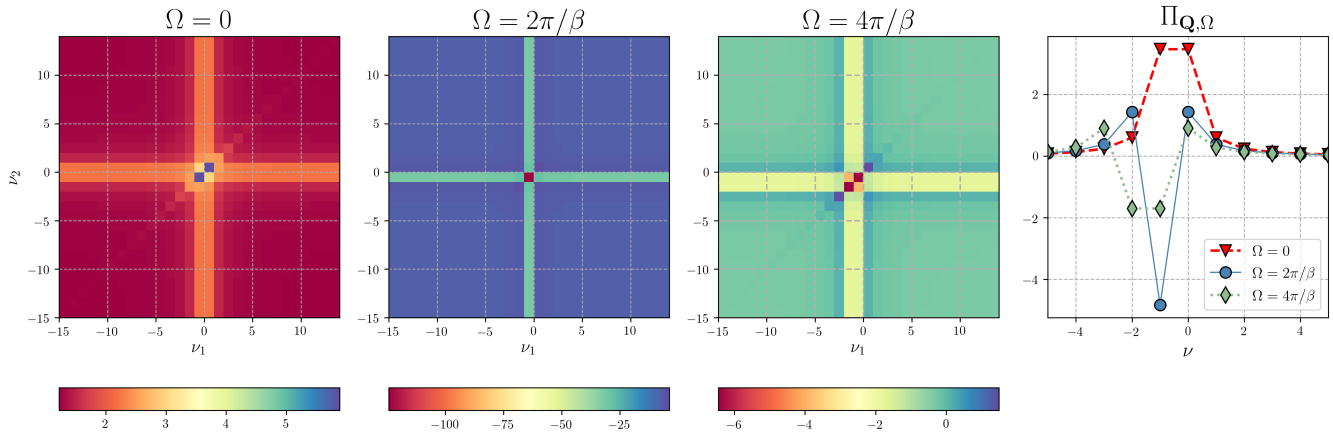

Figure 8: **placeholder**here we will write a lot of useful comments about the figure and I will add a lot of bestemmie

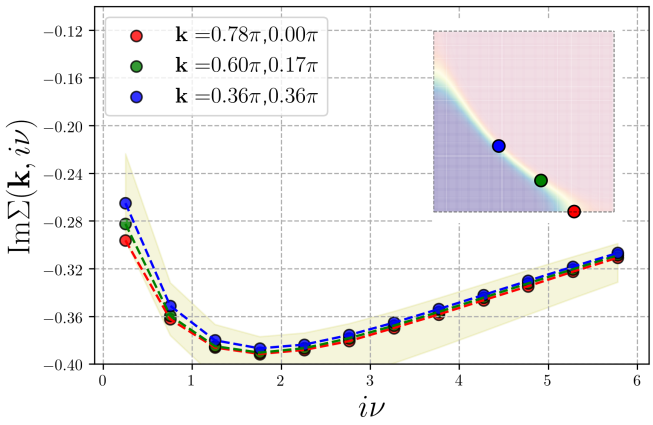

Figure 9: Frequency dependent self-energy for parameter set... . The location of the **k**-point in the Brillouin zone is color coded in the inset.

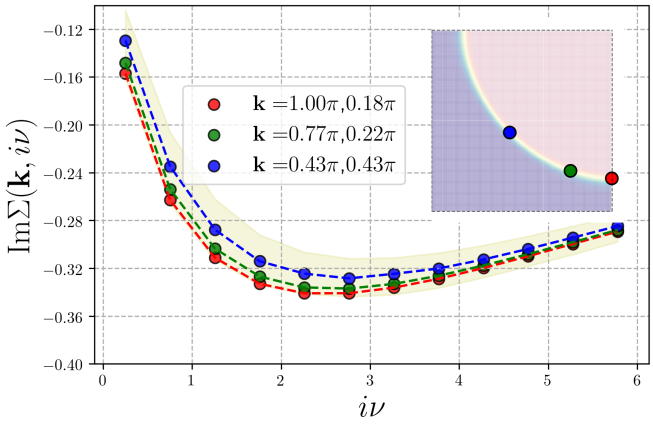

Figure 10: Frequency dependent self-energy for parameter set... . The location of the **k**-point in the Brillouin zone is color coded in the inset.

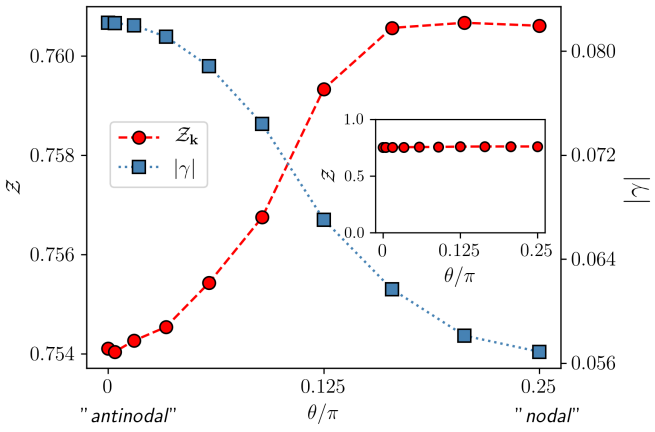

Figure 11: **placeholder**

and:

$$L_{\mathrm{d}\mathbf{Q}}^{\Omega;\nu_1,\nu_3} = -\mathcal{D}_{\mathbf{Q}}^{\Omega;\nu_1,\nu_3} + \frac{1}{2}\int_{\mathbf{p}} (\cos p_x + \cos p_y)\left[\mathcal{M}_{\mathbf{p}}^{\nu_3-\nu_1;\nu_1,\Omega-\nu_1} + \frac{1}{2}\mathcal{M}_{\mathbf{p}}^{\Omega-\nu_1-\nu_3;\nu_1,\Omega-\nu_1} - \frac{1}{2}\mathcal{C}_{\mathbf{p}}^{\Omega-\nu_1-\nu_3;\nu_1,\Omega-\nu_1}\right]. \quad (39)$$

The flow for the $\mathcal{C}$ channel read:

$$\dot{\mathcal{C}}_{\mathbf{Q}}^{\Omega;\nu_1,\nu_2} = \sum_{\nu} L_{\mathrm{c}\mathbf{Q}}^{\Omega;\nu_1,\nu} P_{\mathrm{c},\mathbf{Q}}^{\Omega,\nu} L_{\mathrm{c}\mathbf{Q}}^{\Omega;\nu,\nu_2-\Omega}, \quad (40)$$

with:

$$P_{\mathrm{c},\mathbf{Q}}^{\Omega;\omega} = \int_{\mathbf{p}} G_{\mathbf{p},\omega} S_{\mathbf{Q}+\mathbf{p},\Omega+\omega} + G_{\mathbf{Q}+\mathbf{p},\Omega+\omega} S_{\mathbf{p},\omega}, \quad (41)$$

and:

$$L_{\mathrm{c}\mathbf{Q}}^{\Omega;\nu_1,\nu_2} = U - \mathcal{C}_{\mathbf{Q}}^{\Omega;\nu_1,\nu_2} + \int_{\mathbf{p}} \Big[-2\mathcal{S}_{\mathbf{p}}^{\nu_1+\nu_2;\nu_1,\nu_2-\Omega} + \mathcal{S}_{\mathbf{p}}^{\nu_1+\nu_2;\nu_1,\Omega+\nu_1} \quad (42)$$

$$+ \left(\mathcal{D}_{\mathbf{p}}^{\nu_1+\nu_2;\nu_1,\nu_2-\Omega} - \frac{1}{2}\mathcal{D}_{\mathbf{p}}^{\nu_1+\nu_2;\nu_1,\Omega+\nu_1}\right)[\cos(Q_x) + \cos(Q_y)] \quad (43)$$

$$+ \frac{3}{2}\mathcal{M}_{\mathbf{p}}^{\nu_2-\nu_1-\Omega;\nu_1,\nu_2} + \frac{1}{2}\mathcal{C}_{\mathbf{p}}^{\nu_2-\nu_1-\Omega;\nu_1,\nu_2}\Big]. \quad (44)$$

The flow for the $\mathcal{M}$ channel read:

$$\dot{\mathcal{M}}_{\mathbf{Q}}^{\Omega;\nu_1,\nu_2} = \sum_{\nu} L_{\mathrm{m}\mathbf{Q}}^{\Omega;\nu_1,\nu} P_{\mathrm{m},\mathbf{Q}}^{\Omega,\nu} L_{\mathrm{m}\mathbf{Q}}^{\Omega;\nu,\nu_2-\Omega}, \quad (45)$$

with:

$$P_{\mathrm{m},\mathbf{Q}}^{\Omega;\omega} = \int_{\mathbf{p}} G_{\mathbf{p},\omega} S_{\mathbf{Q}+\mathbf{p},\Omega+\omega} + G_{\mathbf{Q}+\mathbf{p},\Omega+\omega} S_{\mathbf{p},\omega}, \quad (46)$$

and:

$$L_{\mathrm{m}\mathbf{Q}}^{\Omega;\nu_1,\nu_2} = U + \mathcal{M}_{\mathbf{Q}}^{\Omega;\nu_1,\nu_2} + \int_{\mathbf{p}} \Big\{ -\mathcal{S}_{\mathbf{p}}^{\nu_1+\nu_2;\nu_1,\nu_1+\Omega} - \frac{1}{2}\mathcal{D}_{\mathbf{p}}^{\nu_1+\nu_2;\nu_1,\nu_1+\Omega}[\cos(Q_x) + \cos(Q_y)] + \quad (47)$$

$$\frac{1}{2}\left[\mathcal{M}_{\mathbf{p}}^{\nu_2-\nu_1-\Omega;\nu_1,\nu_2} - \mathcal{C}_{\mathbf{p}}^{\nu_2-\nu_1-\Omega,\nu_1,\nu_2}\right]\Big\} \quad (48)$$

[1] J. Hubbard. Electron Correlations in Narrow Energy Bands. *Proc. R. Soc. A*, 276:238–257, November 1963.

[2] W. Metzner, M. Salmhofer, C. Honerkamp, V. Meden, and

K. Schönhammer. Functional renormalization group approach to correlated fermion systems. *Rev. Mod. Phys.*, 84:299–352, January 2012.

[3] C. Platt, W. Hanke, and R. Thomale. Functional renormalization group for multi-orbital fermi surface instabilities. *Advances in Physics*, 62(4-6):453–562, 2013.

[4] C. Wetterich. Exact evolution equation for the effective potential. *Physics Letters B*, 301:90–94, February 1993.

[5] M. Salmhofer and C. Honerkamp. Fermionic Renormalization Group Flows —Technique and Theory—. *Prog. Theor. Phys.*, 105:1–35, January 2001.

[6] Binz, B., Baeriswyl, D., and DouÃğot, B. Wilson's renormalization group applied to 2d lattice electrons in the presence of van hove singularities. *Eur. Phys. J. B*, 25(1):69–87, 2002.

[7] B. Binz, D. Baeriswyl, and B. DouÃğot. Weakly interacting electrons and the renormalization group. *Annalen der Physik*, 12(11-12):704–736, 2003.

[8] F. B. Kugler and J. von Delft. Multiloop functional renormalization group that sums up all parquet diagrams. *ArXiv e-prints*, March 2017.

[9] G. Rohringer, A. Valli, and A. Toschi. Local electronic correlation at the two-particle level. *Phys. Rev. B*, 86(12):125114, September 2012.

[10] C. Husemann and M. Salmhofer. Efficient parametrization of the vertex function, Ω scheme, and the t,t$'$ Hubbard model at van Hove filling. *Phys. Rev. B*, 79(19):195125, May 2009.

[11] C. Husemann, K.-U. Giering, and M. Salmhofer. Frequency-dependent vertex functions of the (t, t') hubbard model at weak coupling. *Phys. Rev. B*, 85:075121, Feb 2012.

[12] J. Lichtenstein, D. SÃąnchez de la PeÃśa, D. Rohe, E. Di Napoli, C. Honerkamp, and S.A. Maier. High-performance functional renormalization group calculations for interacting fermions. *Computer Physics Communications*, 213:100 – 110, 2017.

[13] N. Wentzell, G. Li, A. Tagliavini, C. Taranto, G. Rohringer, K. Held, A. Toschi, and S. Andergassen. High-frequency asymptotics of the vertex function: diagrammatic parametrization and algorithmic implementation. *ArXiv e-prints*, October 2016.

[14] C. Karrasch, R. Hedden, R. Peters, T. Pruschke, K. Schönhammer, and V. Meden. A finite-frequency functional renormalization group approach to the single impurity Anderson model. *J. Phys.: Condens. Matter*, 20:H5205, August 2008.

[15] C. Taranto, S. Andergassen, J. Bauer, K. Held, A. Katanin, W. Metzner, G. Rohringer, and A. Toschi. From Infinite to Two Dimensions through the Functional Renormalization Group. *Phys. Rev. Lett.*, 112(19):196402, May 2014.

[16] C. Honerkamp, D. Rohe, S. Andergassen, and T. Enss. Interaction flow method for many-fermion systems. *Phys. Rev. B*, 70(23):235115, December 2004.

[17] Nils Wentzell, Serge Florens, Tobias Meng, Volker Meden, and Sabine Andergassen. Magneto-electric spectroscopy of andreev bound states in josephson quantum dots. May 2016.

[18] A. Eberlein. Fermionic two-loop functional renormalization group for correlated fermions: Method and application to the attractive Hubbard model. *Phys. Rev. B*, 90(11):115125, September 2014.

[19] N. D. Mermin and H. Wagner. Absence of ferromagnetism or antiferromagnetism in one- or two-dimensional isotropic heisenberg models. *Phys. Rev. Lett.*, 17:1133–1136, Nov 1966.

[20] Tobias Baier, Eike Bick, and Christof Wetterich. Temperature dependence of antiferromagnetic order in the hubbard model. *Phys. Rev. B*, 70:125111, Sep 2004.

[21] The equation for the particle-particle channel is slightly different from the one usually reported in fRG, see, e.g., Ref. 10. This is because we took $V^\Lambda = V^\Lambda_{\uparrow\downarrow\uparrow\downarrow}$ instead of $V^\Lambda = V^\Lambda_{\uparrow\downarrow\downarrow\uparrow}$.